IV Data Analysis

The process of converting the measured data into a differential $(e, e'pp)$ cross section can be divided in several parts. First, particles are identified and their momentum and relative timing are determined, using the raw data obtained from each detector. Subsequently, the number of real events is determined as a function of one or more kinematic quantities. After normalization and correction for detection volume, cross sections are obtained. This chapter is devoted to the methods used in this analysis. At the end, an estimate of the systematic uncertainty associated with the determined cross sections is presented.

4.1 Analysis of QDQ data

The event information obtained from the QDQ magnetic spectrometer contains hit-pattern information from the four MWDCs and 12 timing scintillators, and ADC information from the aerogel Čerenkov detector. The matrix-formalism described by de Vries *et al.* [Vri90] is used to reconstruct the vertex position (y_{tg}) and the momentum vector of the scattered electron at the target. A suitable set of matrix elements for use with an extended target was determined earlier by Spaltro [Spapc]. Additional data collected in this experiment were used to verify and improve this set of matrix elements. Several matrix elements were adjusted to reflect the alignment conditions of this experiment.

The y_{tg} reconstruction was verified using the known dimensions of the barrel cell. At an angle of 27°, the entire length of the cell is within the y-acceptance of the QDQ. The diameter of the cell, as determined from the top-to-top distance in Fig. 4.1, was found to be 47±0.8 mm, which is reasonably close to the actual value of 50 mm.

Using sieve-slit measurements performed with the ^{3}He target cell, the correlation between y_{tg} and the in-plane scattering angle ϕ was verified. Using the known calibration for y, the first-order (y, ϕ) and the zeroth-order ϕ matrix element were adjusted. The resulting set of matrix elements was checked

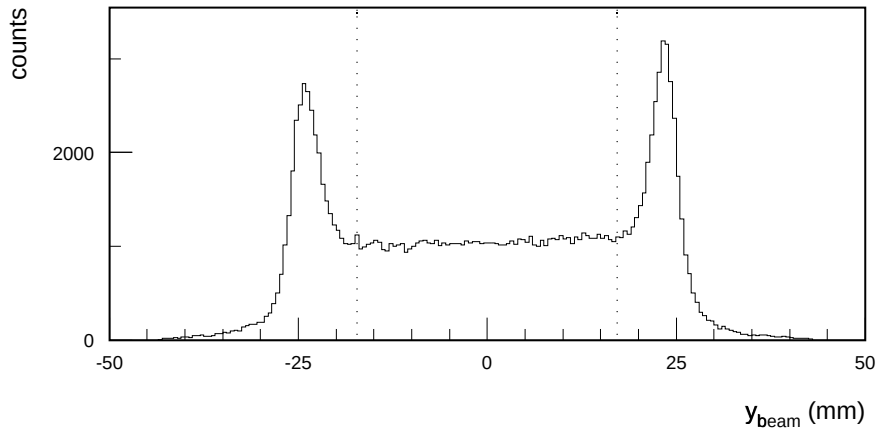

Figure 4.1: *The y_{tg} reconstruction, corrected for the angle of the QDQ. The dashed lines indicate the projection of the cut, used in the analysis, to reject events from the cell walls. They correspond to a y_{tg} position of ± 8 mm. (data: LQA)*

with several sieve-slit measurements taken on ^{12}C and ^{3}He, at various moments during the experiment.

The time-of-flight reconstruction of the electrons, obtained from the matrix elements determined by Spaltro [Spapc], was verified using the time-difference distribution of two-fold coincident events from this experiment. As the phase of the QDQ detector trigger is defined by combining the logic signals from twelve different regions in the detection plane, off-line corrections have to be applied to synchronize events originating from these different regions. They are determined employing the time differences of two-fold coincident events and the hit-pattern information contained in the QDQ event fragments. The timing corrections applied are all less than 3 ns.

Besides electrons, also negatively charged pions and muons will reach the detection system of the QDQ. Therefore, information from the aerogel Čerenkov detector is used to suppress the contribution from these particles. With the index of refraction n=1.05, pions and muons with momenta below 440 MeV/c and 330 MeV/c respectively will not generate Čerenkov light in the aerogel.

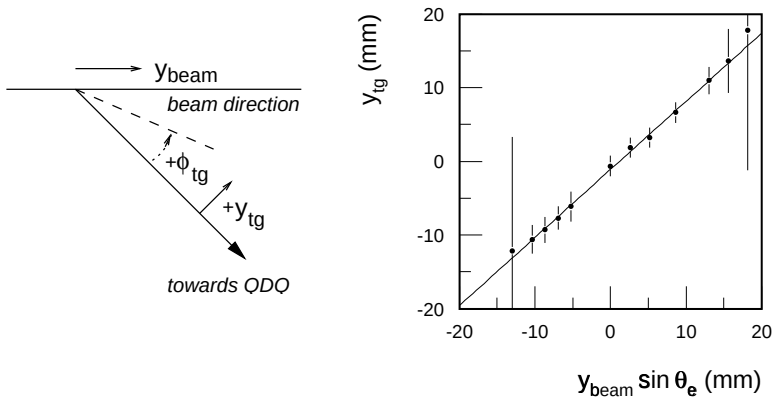

Figure 4.2: *Calibration of the y_{tg} reconstruction based on the data collected with a slanted target. The QDQ angle, $\theta_{e'}$, was 60°. Error bars indicate the width (FWHM) of the reconstructed y distribution. The coordinate system used for the QDQ matrix element formalism is shown on the left-hand side.*

The probability that an electron will not generate a signal in the Čerenkov detector is estimated to be below 1.7×10^{-4} [Sch97]. Due to the finite resolution with which the signals from the Čerenkov PMs are digitized, an additional inefficiency is introduced in the analysis by requiring that the measured ADC value is different from zero. The additional loss is estimated to be less than 0.5%.

The Y-dependence of the (θ, ϕ) acceptance

The angular acceptance of the QDQ as a function of y – the distance between the vertex position and the optical axis, as seen on a line perpendicular to this optical axis, shown in Fig. 4.2 [Vri90] – is only flat between -3 and $+6$ mm [Spa97]. To verify this range and to investigate the (θ, ϕ) acceptance for y positions outside this region, measurements were performed with a slanted copper strip target. With such a setup, the target height is correlated with the vertex position along the beam line (y_{beam}). Measurements were performed for twelve different vertex positions between $-21 < y_{beam} < 15$ mm. The QDQ spectrometer was positioned at $-60°$ and the '70x70' slit was used. This slit has an octangular shape and an

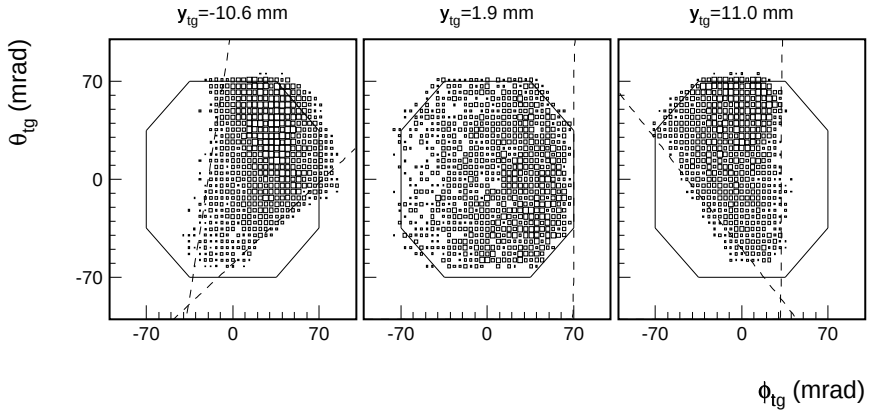

Figure 4.3: *Filling of the QDQ solid angle for three values of y_{tg}. The octagonal shape indicates the nominal acceptance of the '70x70' slit. The dashed lines represent the parametrization of the acceptance as used in the analysis (see text). The data shown were obtained with the slanted target.*

angular acceptance of ± 70 mrad for both the in-plane and out-of-plane angle. It is located at 481.5 mm from the target.

The various data sets are used to verify the y_{tg} reconstruction, as this is a prerequisite for using y_{tg} in the analysis of extended-target data. Figure 4.2 shows the reconstructed y_{tg} as a function of the nominal y-position as determined from the measurement of the slanted-target height. The contraction of y as determined from the slope is 1.06 ± 0.04, which is identical to the value obtained from the cell wall measurement.

To determine the acceptance of the QDQ as a function of y_{tg}, two-dimensional plots of the (θ, ϕ) distribution are parametrized using cutoff lines in the (θ, ϕ)-plane which depend on y_{tg}. The parameters are determined on basis of both the slanted-target data and data obtained with the barrel cell during this experiment. To adequately describe the acceptance, two sets of straight lines in the (θ, ϕ)-plane are needed, one for each side of the acceptance ($y_{tg} < 0$ and $y_{tg} > 0$ mm, respectively). The effect of y_{tg} on the acceptance, as well as the parametrization are indicated in Fig. 4.3. The effective acceptance described by this method

is used to calculate the contribution of the QDQ to the detection volume as described in section 4.4.

Limitation imposed on the spectrometer data

All coincidence measurements on ^{3}He were performed with the '70x70' slit. The out-of-plane acceptance, θ_{tg}, is reduced further by geometric limitations inside the QDQ to $\theta_{tg} > -60$ mrad. Software limitations on θ_{tg} or ϕ_{tg} were imposed during the analysis at ± 150 mrad to eliminate events not originating from the target.

In the analysis of the coincidence data, the acceptance in y_{tg} has been limited to $-8 < y_{tg} < 8$ mm. This is well inside the region were the reconstruction of y_{tg} can be assumed to be reliable (based on the information in Fig. 4.2). The cut is also sufficient to reduce to contribution of cell-wall events to the coincidence data below the 1.4% level for all kinematic settings (see section 4.3).

Due to geometrical limitations, part of the focal plane cannot be reached by particles without obstruction. Therefore, the useful range of X1 has been limited in the analysis to $528 < \mathrm{X1} < 4200$ fine-channels – a momentum acceptance of 9.5% – as determined from a quasi-white spectrum measured at the LQ kinematic setting.

Detection efficiency

The efficiency of the QDQ spectrometer is determined by various ingredients: the electron detection efficiency of the wire chambers, scintillators, the frontend electronics, the detector trigger and the reconstruction efficiency in the off-line analysis.

The MWDC and scintillator efficiencies were optimized at the beginning of the experiment. A fixed dead time of 500 ns has been introduced to ensure proper event readout; a prompt trigger output with negligible dead time is provided to determine the fraction of events lost. The trigger live time during the experiment was better than 99.5%.

The variation of the detection efficiency as a function of focal-plane position was investigated by performing (e, e') scattering experiments on ^{12}C, such that the peak corresponding to elastically scattered electrons was located at different

positions along the focal plane. For each measurement, the cross section was determined. Relative variations between the various measurements were found to be less than 1%.

The absolute detection efficiency was determined using elastic scattering from ^{12}C at different spectrometer angles. The collected charge was determined, taking into account the duty-factor dependence of the beam current measurement. The measured cross sections were compared to calculations based on a 15-parameter Fourier-Bessel parametrization of the charge distribution [Vri87]. The efficiency was found to be 96% [Lappc, Sta99b]; the statistical and systematic uncertainties amount to 2% and 3%, respectively.

4.2 Analysis of HADRON data

The procedure to convert raw event fragments, originating from the HADRON readout electronics, to proton momentum vectors is similar for both detectors used.

Determination of proton momenta

The methods employed to convert the measured ADC information to the light produced in the scintillator at the impact point, as well as the way to treat particles impinging on the detector under different impact angles are already extensively described elsewhere [Lee96, Ond98b, Sta99b]. In summary, the effective gain of the photomultiplier (PM) is determined by comparing ADC distributions measured in subsequent layers with light-production calculations based on the Bethe-Bloch energy-loss formula and the energy-to-light parametrization due to Wright [Wri53]. The attenuation along the scintillators is accounted for by determining the response at various values of the distance from impact point to PM. For the horizontally segmented layers the impact position relative to the PM is obtained from the perpendicularly segmented hodoscope H2. For the calibration of H2 itself, selections are made based on L1. The light yield estimate is phenomenologically corrected for impact-angle effects. Using this procedure, an effective quantity L_{norm}, labelled 'normalized light', is obtained.

Particle identification

The identification of proton events in the detector is performed in two steps. Firstly, tracks are identified using the procedures described in, *e.g.*, [Lee96], where it should be noted that no self-timing restrictions on L1 are imposed in the analysis to avoid ambiguity in determining the correction for 'cross-over' events in this layer [Kas97]. Secondly, based on the amount of normalized light in the stopping layer, the estimated amount of light a proton should have produced in the preceeding layer is calculated. The difference, ΔL, between this calculated amount of light and the measured yield results in a distribution which peaks around zero for protons. A window on ΔL is used to suppress non-proton events in the analysis. This gate is set in such a way that more than 99% of the protons will be identified correctly, which however implies that a fraction of the non-proton events will incorrectly be flagged as proton. These events are eliminated after subtraction of the accidental coincidences (see section 4.3).

Timing corrections

In the analysis, the arrival time of the HADRON detector trigger, as measured by the CD, is corrected for time-of-flight of the proton and for various time-differences occurring in the proton detection system. In this way, the departure time of the proton at the vertex is determined,

$$t_{dep} = t_{\mathrm{ATR}} - t_{tof}(T_p, \alpha) - t_{walk}(\mathrm{ADC}) - t_{prop}(i_{\mathrm{H2}}) - t_{off}(i_{\mathrm{L1}}), \qquad (4.1)$$

using a phenomenological method to account for effects on the time-of-flight that depend on the impact angle α. The determination and use of the various correction factors are described in, *e.g.*, [Sta99b]. The total effect of the timing correction varies between 4 and 18 ns, primarily determined by the time-of-flight correction (4 to 11 ns).

The correction factors partially depend on the calibration parameters used in the energy determination. As these parameters were optimized for each kinematic setting separately, also the timing corrections were determined on a per-kinematics basis. The optimal resolution obtained is 0.72 ns (FWHM) for data taken at the one-hour time scale. A typical coincidence time distribution is shown in Fig. 4.4.

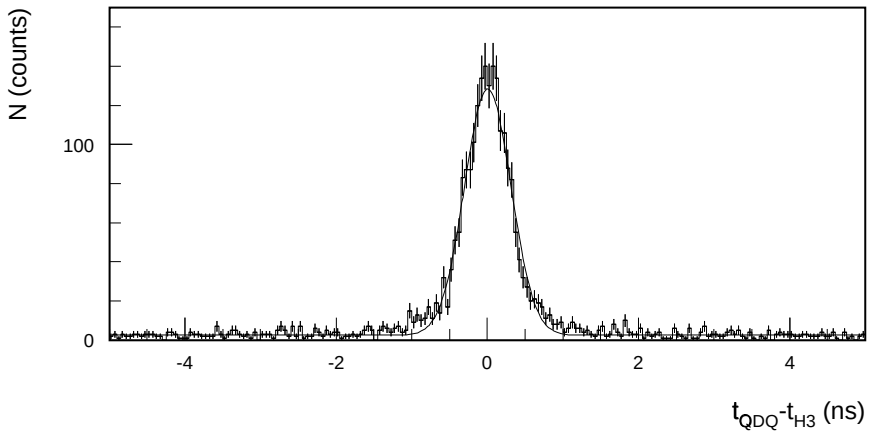

Figure 4.4: *Time-difference distribution for two-fold coincidental events QDQ–HADRON3. The resolution amounts to 0.72 ns FWHM. (data: LQV, taken over a period of one hour)*

Long-term variations of the peak position in the coincidence time distribution were observed for data taken in a single kinematic setting. This effect, which occurs at a time scale of several days, deteriorates the resolution and thereby reduces the real-to-accidental ratio. Only the time-difference distribution for QDQ–HADRON3 coincidences is subject to this problem, which suggests it is due to the readout electronics of HADRON3 being located far away (60 m) from the detector proper, whereas the readout systems for QDQ and HADRON4 are located within several metres from their respective detection systems. As the real-to-accidental ratio for QDQ–HADRON3 coincidences is extremely good and variations are not more than 0.7 ns, this effect was taken into account by choosing wider time-difference windows in the coincidence analysis; the real-to-accidental ratio for $(e, e'pp)$ events is primarily determined by the ratio for QDQ–HADRON4 coincidences, which was not affected.

Detection efficiency

The efficiency of the HADRON detector is determined by various effects: electronics live time, deficiencies in the reconstruction procedure, and by multiple-

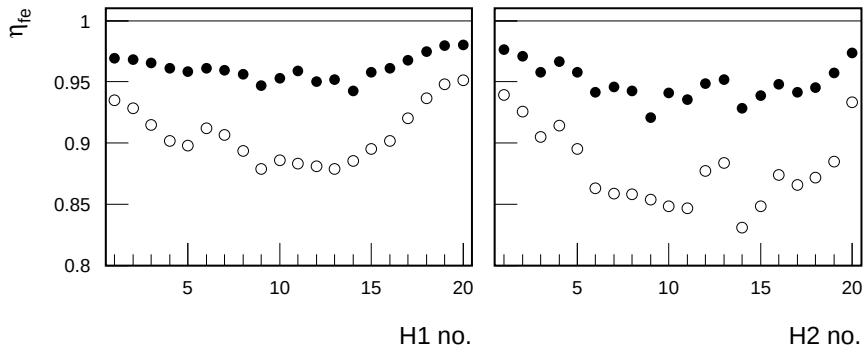

Figure 4.5: *Live time of the frontend electronics of HADRON4 for both hodoscope layers, when a hit from both sides of any element is required. Data were taken at two different values of the luminosity. The solid dots correspond to an average current of 0.5 μA, the open dots to 1.5 μA. (Data: LQA)*

scattering and hadronic interactions of the protons in the detector. The efficiencies are monitored during the experiment or estimated using a model-description of the detector. Independent checks are performed using the kinematically overdetermined $^1\mathrm{H}(e, e'p)$ reaction and by performing measurements at the same kinematic setting, but at different luminosities.

As described in section 3.4, the live time of the frontend electronics is determined using test pulses as a monitor This live time depends on the instantaneous luminosity and is therefore determined on a per-file basis. The influence of luminosity variations is illustrated in Fig. 4.5. The live time is lowest in the two hodoscope layers. The fluctuations among elements within the same layer are due to variations in the solid angle subtended by the elements (which decreases as the elements are located further away from the detector heart line), to the frontend thresholds set and to the angular dependence of the singles count rate.

Since multiple frontends are involved in the detection of a particle track, the *track live time* is determined as the product of the live times of the frontends that are part of the track. In using this method, a small overcorrection will result from correlated frontend live times. As the main contribution to the track live

time is due to the hodoscopes (which are oriented perpendicular to each other and are therefore hardly correlated), and the frontend live time of the stopping layers is close to 100%, the effect of correlated dead time to the track live time is estimated to be less than 1%.

Also with the detector trigger a live time is associated, which like that of the frontends, depends on the luminosity. This inefficiency is determined by measuring the number of prompt triggers (which have a negligible dead time) and the number of generated detector triggers (ATRs). The trigger live time – the ratio ATR over prompt triggers – amounts to about 85%. It is recorded on a file-by-file basis and used as such in the analysis.

To avoid ambiguities in the reconstruction of particle tracks and in the timing corrections to be applied to the arrival time of the detector trigger, those events in which more than one element of L1 fired (multiple-hit, MH) are disregarded in the analysis. Also tracks in which more than one of the H1 candidate elements was hit, are ignored. A count of the number of MHs in L1 is kept. As in almost all cases (97%) MHs are due to particles crossing the edge between two neighbouring L1 elements (cross-overs), the efficiency is determined to be

$$\eta_{\mathrm{MH}}(i_{\mathrm{L1}}) = 1 - \frac{1}{2}\frac{n_{\mathrm{MH}}(i_{\mathrm{L1}})}{n_{event}}. \tag{4.2}$$

Here $n_{\mathrm{MH}}(i_{\mathrm{L1}})$ is the number of MHs in the i-th element of L1, and n_{event} the total number of events detected. The correction is determined and applied to the data on a per-file basis.

An additional inefficiency and source for possible misreconstruction of detected protons are interaction processes occurring in the flight-path of the particles, especially in the shielding material.

Firstly, hadronic interactions among the impinging protons and nuclei in the shielding and scintillator material will occur. The energy loss suffered due to both elastic and inelastic scattering may be so large, that the protons subsequently fail to reach L1 and thus will not generate a trigger, a process which will primarily affect protons with energies near the detection threshold. Energy losses can also result in loss of a proton – when it fails the particle identification procedure – and lead to misreconstruction of its incident energy.

Secondly, multiple-scattering may lead to extremely large angular variations in such a way that the proton either escapes from the detector at the sides or is stopped outside the candidate array used in the analysis. These proton tracks will not be reconstructed by the analysis procedure.

To account for the aforementioned inefficiencies, a model description of both HADRON detectors is made using the detector description and simulation tool GEANT [Gea94]. In this model, the geometries of the target system and scattering chamber, and the description of the detector housing and scintillator package are implemented. Using the simulation capability of GEANT, protons with a uniform energy and angular distribution are generated within a solid angle slightly larger than the one spanned by the detector collimator. The vertices are also uniformly distributed over a line of 50 mm along the beam path to account for the extension of the target. The light output of all elements is simulated and subsequently converted to ADC values. For this conversion, gain parameters as determined from the real data are used. The digitized values are stored in a pseudo-event format compatible with the one produced by the event builder.

The generated pseudo-data are treated like regular data in the analysis procedure. The efficiency due to interaction processes is defined as the number of protons accepted by the analysis procedure over the number of generated particles. This efficiency is dependent on the proton energy and on the impact angle of the particles on the detector (and thus the effective thickness of material seen). The correction factors are therefore determined for intervals in T_p and impact angle α of 5 MeV and 1°, respectively.

Care should be taken not to implicitly apply the MH correction twice, as most MHs are cross-over events due to real protons. The efficiency is therefore separated in two parts. The hit-efficiency η_{hit} is defined as the probability that a proton, originating form the target, will reach H1. The reconstruction efficiency η_{rec} measures the probability that a proton, which hits only one L1 element and one of the corresponding H1 elements, is properly identified as such by the analysis procedure. The product of these two efficiencies is applied as a correction factor to the data.

The amount of light produced by protons in the stopping layer may remain below the detection threshold. In this case, the analysis procedure will incorrectly identify the previous layer as the stopping layer and an attempt will be

Table 4.1: *Overview of* ^{1}H$(e,e'p)$ *measurements performed with HADRON3. The variable* η_{total} *is the ratio of the number of measured protons over the expected yield, after all corrections have been applied to the HADRON data. The uncertainties shown are statistical only.*

file ID	$\theta_e(^\circ)$	$\theta_p(^\circ)$	T_p (MeV)	$\eta_{hit\cdot rec}$	η_{trig}	η_{MH}	η_{total}
464	47	54	90	0.91	0.92	0.91	95.6±2.9%
465	47	54	90	0.91	0.92	0.91	95.4±2.7%
466	47	60	90	0.91	0.94	0.92	97.3±2.9%
468	47	60	90	0.91	0.94	0.92	101.3±3.1%
469	57	54	120	0.86	0.92	0.92	99.0±3.7%
470	57	54	120	0.86	0.92	0.92	97.8±3.6%

made to determine the identity of the proton under this false assumption. The windows used for the particle identification are sufficiently wide to accept these events and no protons will be lost. However, the reconstructed energy will be slightly too small. This redistribution will deteriorate the resolution, but will not cause loss of yield for the $(e,e'pp)$ events under study.

Verification of the efficiency correction

Verification using the reaction ^{1}H$(e,e'p)$

To verify the efficiency corrections applied to the HADRON singles data, measurements were performed with a hydrogen target. As the ^{1}H$(e,e'p)$ reaction is kinematically overdetermined and the acceptance of the HADRON detector is much larger than the proton cone corresponding to the acceptance of the QDQ electron spectrometer, every elastically scattered electron inside the QDQ acceptance should lead to a proton being detected in HADRON. During this experiment, ^{1}H$(e,e'p)$ measurements were performed with the QDQ and HADRON3 under three different kinematic conditions, listed in Table 4.1. The target cell used for the ^{1}H$(e,e'p)$ measurements is identical to the one used during the ^{3}He$(e,e'pp)$ measurements. The density of the hydrogen gas was 0.34 mg/cm^3.

As the energy of the emitted protons is strongly dependent on the scattering angle of the electron, the QDQ acceptance was limited to ±20 mrad in-plane,

± 30 mrad out-of-plane and a y_{tg} acceptance of ± 4 mm. The energy distribution of the scattered electrons was corrected for energy variations due to the finite angular acceptance (*kinematic correction*). A cut of ± 4 MeV was used around the peak in the electron energy distribution to eliminate events which suffered a large energy loss due to radiative effects.

The corrections applied to the HADRON data are determined in a way identical to that for $(e, e'pp)$ data. Trigger, frontend and MH correction factors are determined on a per-file basis. The model-dependent efficiencies (η_{hit} and η_{rec}) are taken from a simulation with a ^{3}He gas target. Although the density of the hydrogen gas is much lower, this change has only minor influence on the correction factors calculated.

No accidental coincidences are observed in the time difference distribution for QDQ–HADRON3 events. The total reconstruction efficiency η_{total} is thus determined directly from the corrected number of reconstructed protons. Besides the statistical error quoted in Table 4.1, a systematic error of 4% has to be associated with these measurements due to uncertainty in the detector simulation and correlated *track* live time (see section 4.6). As the reconstructed efficiency is compatible with one within the statistical and systematic error, no additional correction factor was applied to the ^{3}He$(e, e'pp)$ measurements.

Verification by luminosity variations

As some sources of inefficiency depend on the instantaneous luminosity (track live time and trigger live time), the validity of their corrections can be investigated by repeating the measurements at different values of the luminosity. The test was performed during the measurement of LQA, as this setting features the highest count rate. In Fig. 4.6, the number of fully corrected, true three-fold coincident $(e, e'pp)$ events per unit charge is displayed for all datafiles measured at LQA. All conditions, except the incident beam current, are kept constant. Data files up to and including no. 334 were measured with an incident current of 1.5 μA; the current was changed to 0.5 μA from file 335 onwards. The correction factor applied to the data varies from 1.95 at the high current to 1.25 at the low current measurements. The reconstructed numbers of true $(e, e'pp)$ events per unit charge are consistent: 174 ± 2.8 and 178 ± 3.9 at an incident beam current of 1.5 and 0.5 μA, respectively.

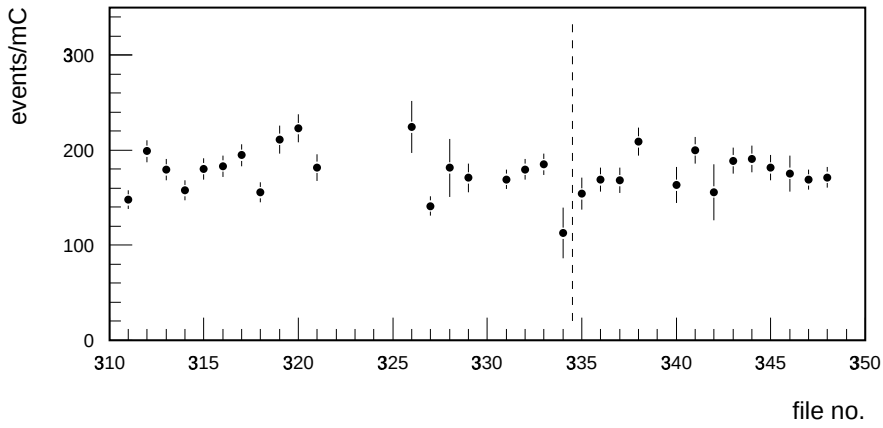

Figure 4.6: *Number of true $(e, e'pp)$ events per unit charge, as determined on a file-by-file basis for the LQA kinematic setting. All correction factors described have been applied to the data. The dashed line indicates the change in luminosity from 1.5 μA up to file no. 334 to 0.5 μA from file no. 335 onwards.*

Recuperation of lost H2 information in the LW kinematics

During the measurement of the LW kinematic setting, the combination process of sub-event fragments in the HADRON4 data acquisition chain occasionally selected the wrong sub-event in one specific crate out of the four. This crate contained all but three digitizer modules for H2, the hodoscope layer sensitive to the out-of-plane direction. No digitizers from other layers were contained in this crate.

In 20% of the cases the sub-event supplied by this crate did not belong to the requested event, but to an uncorrelated other event. The problem became apparent during the frontend efficiency determination, which showed a 20% reduced efficiency for a number of elements, all located in the same crate. This is illustrated in Fig. 4.7. Such an effect is only visible for test pulses and laser events as these show a characteristic hit pattern throughout the complete detector. It can safely be assumed that this miscollection of sub-events also affected the regular data. As it cannot be determined which events are affected, all in-

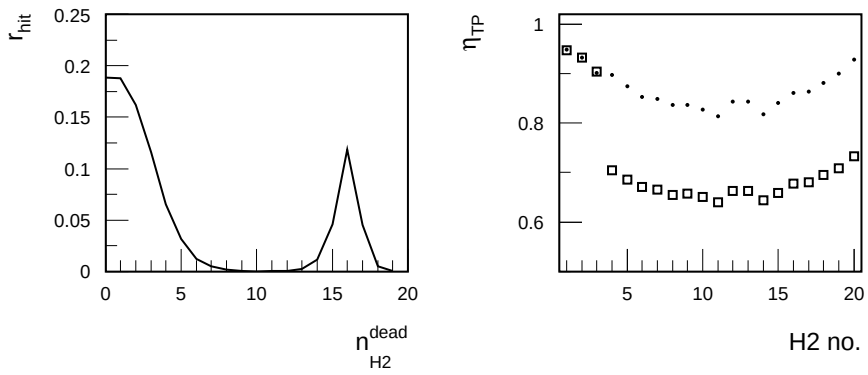

Figure 4.7: *The effect of event miscollection on the frontend live time. The left panel shows the frequency distribution of the number of non-responding H2 elements per test pulse event. The right panel shows the apparent frontend live time. Open squares represent the estimated live time determined using all test pulse events, the solid dots using only those test pulse events in which at least 10 elements are alive,* i.e.*, those in the peak on the left-hand side in the left panel. (Data: LW, file 715)*

formation originating from this crate had to be discarded in the analysis. To retain consistency among all analysed events, also the information originating from the three unaffected H2 elements was discarded.

The H2 impact information is used in the analysis for several purposes: *i)* in the gain determination for the elements of all other, vertically mounted, layers via the attenuation, *ii)* in the timing corrections by the propagation-time parametrization, *iii)* in the determination of the out-of-plane angle of the proton momentum vector, *iv)* for identification of protons stopping in L1; here, the exact ADC values of the H2 elements are needed.

As the miscollection problem was present in more than 90% of the measurements performed at the LW settings, it was considered worthwhile to try to recover the lost H2 information. A partial reconstruction of the out-of-plane information is possible because of the double-sided readout of the perpendicularly mounted hodoscope plane H1. Propagation time differences within the elements

of H1 are used to reconstruct the impact position with an accuracy of about 50 mm.

The ADC information of H2 is permanently lost and therefore no particle identification can be performed for protons stopping in L1. In the analysis for LW, these protons are therefore not used. This raises the effective proton-detection threshold to protons stopping in L2. Taking into account the 1.0 mm steel shielding used during LW, the threshold becomes 53 MeV (compared to 36 MeV for L1 stoppers). The remainder of this section will be concerned with the method developed to recover the H2 hit-information.

The method to reconstruct the out-of-plane information proceeds in several steps:

- Parametrize the propagation-time difference for each H1 element, such that the time difference can be used to calculate the corresponding H2 element number. Use the reconstructed H2 number to perform light-attenuation corrections, timing correction and determination of the out-of-plane angle.
- Determine the additional frontend live time of every H1 element. In the regular analysis, only one of the two H1s needs to fire in order to obtain a valid event. As both are needed now to do the H2 reconstruction, an additional live time has to be corrected for.
- Determine the efficiency of this procedure using data files with valid H2 information.

The data produced by the frontend electronics contain the difference between hit arrival time and the arrival of the time-stop signal from the global detector trigger. This time-stop signal has a fixed time relation to the hit arrival time in the L1 element. If we consider valid events, only one L1 and one H1 strip are involved in the event. In this case, the difference in arrival time between the two sides of H1 is correlated with the impact position due to the propagation time of the light inside the scintillator.

The correspondence between H1 time difference and the H2 impact position was determined for each H1 strip separately. A plot of the relation between Δt_{H1} and the H2 number is shown in Fig. 4.8. This relation was parametrized with a straight line and used in the analysis of the affected files. The difference between

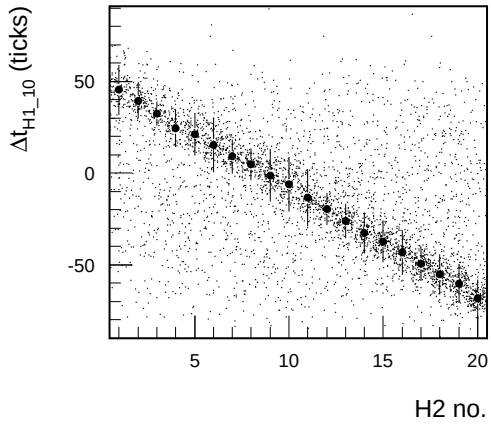

Figure 4.8: *Time difference between hits arriving on the top-side and bottom-side PM of an H1 element as a function of the element number as determined in the regular-type analysis. The error bars indicate the width (FWHM) of the time difference distribution. (Data: IW, file 685)*

the H2 number determined with this procedure as compared to the regular one is displayed in Fig. 4.9.

The detector trigger for HADRON4 is a coincidence between a hit in an L1 element and a hit in any of the four corresponding H1 PMs. In the regular analysis, the only additional requirement is that just one H1 strip was hit. It is therefore not necessary that both sides of this H1 element have a valid signal.

However, to perform the H2 reconstruction, a signal from both sides of the H1 strip is required. This induces an additional inefficiency, corresponding to the ratio of the live time for the H1 element, when requiring a signal from both frontends, compared to the live time for this H1 element when only one frontend is required. This additional live time effect is determined per H1 strip and amounts to 92.7% on average.

For several files from IW, the effectiveness of this alternative procedure is determined using HADRON4 single events. Only true protons stopping in L2 and beyond are taken into account in the comparison. The amount of true

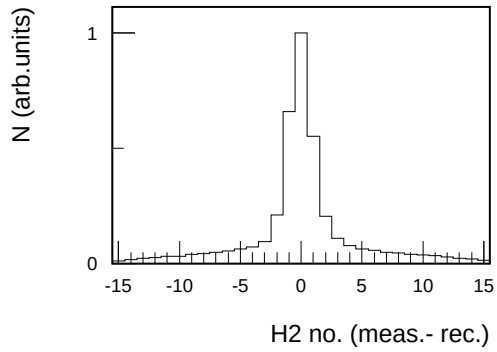

Figure 4.9: *Difference between the tracking H2 element as determined by the regular analysis and by using H1 time difference information. (Data: file 685)*

protons recovered is 99.4±0.8%. It is therefore assumed that this reconstruction procedure is sufficiently accurate to be used in the analysis of the $(e, e'pp)$ events.

4.3 From counts to yield

As described earlier in section 3.5, the differences in the arrival times of the various detector triggers are used to discriminate the different types of events: single events, two-fold coincidences among the various detector combinations, and three-fold coincident events. Within the coincidence detector these different event types are selected by time difference. A time difference of ±125 ns between every pair is allowed for by the coincidence detector (CD).

The arrival times measured by the CD are corrected for detector-dependent timing corrections to yield the departure times of the particles from the vertex. For the events flagged as three-fold coincident by the CD, the difference in the departure time between the electron trigger and the proton in either forward (H3) or backward (H4) direction is shown in Fig. 4.10.

In this figure, several kinds of events can be discriminated. The peak, located at a time difference of 0 ns for both combinations, corresponds to real three-fold coincidences. The two ridges at Δt_{QH4}=0 ns and Δt_{QH3}=0 ns are due to real $(e, e'p)$ coincidences between the scattered electron and either the

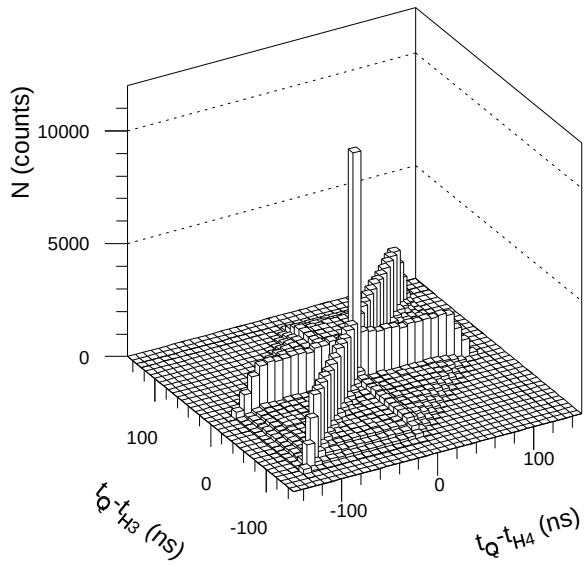

Figure 4.10: *Time difference distribution for three-fold coincident events. The binning has been chosen to enhance visibility and does not reflect the resolution with which the distribution was measured. The resolution amounted to 1.5 ns (FWHM). (Data: LQA)*

backward or forward proton detector together with an accidental third. The ridge at $\Delta t_{\mathrm{QH4}} = \Delta t_{\mathrm{QH3}}$ contains real two-proton coincidences together with an accidental electron trigger. The structures are located on a flat background of events that are three-fold uncorrelated.

To extract the true $(e, e'pp)$ events, the contributions of the flat background and the ridges to the region of the real coincidences has to be estimated. This is best performed by symmetrizing the coincidence time spectrum by a linear transformation

$$\tau_x = \frac{1}{\sqrt{3}} \left(2t_{\mathrm{H4}} - t_{\mathrm{Q}} - t_{\mathrm{H3}}\right) \tag{4.3}$$

$$\tau_y = \left(t_{\mathrm{Q}} - t_{\mathrm{H3}}\right). \tag{4.4}$$

After this transformation, the time difference distribution will exhibit a symmetric hexagonal shape as displayed in Fig. 4.11. The width b is chosen in such a

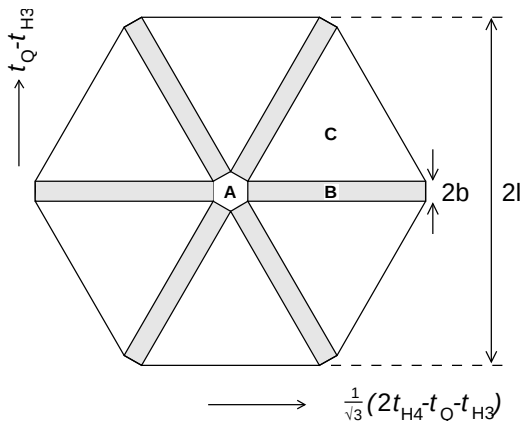

Figure 4.11: *A hexagonal shape is obtained after the coincidence time distributions are symmetrized.*

way that the full width of the two-fold coincidence band is well within the regions B. As the coincidence time resolution is always better than 1.5 ns (FWHM), b was chosen to be 3 ns, *i.e.*, at least 4.5σ from the peak. The value of l determines the accuracy with which the accidental level inside the real region A can be estimated. The accuracy is largely determined by the statistical uncertainty on the two-fold coincident events in the B regions, as these will contribute most to area A. The length l was chosen to be 60 ns. This is still well within the acceptance of the CD.

The number of true $(e, e'pp)$ events is determined by the number of events in region A, reduced with the estimated contribution from B and C,

$$N_T = N_A - f_B N_B - f_C N_C, \tag{4.5}$$

where the fractions f_B and f_C are derived from the lengths and areas of the regions A, B, and C [Ond98b, Sta99b]. The fractions f_B and f_C are subsequently used as weights in the summation of the events. Events outside the regions A, B and C are discarded.

Contributions from cell walls

The ^{3}He target, described in section 3.2, is a cylindrically shaped container made of aluminium with a diameter of 50 mm. Hence, the cell walls will be

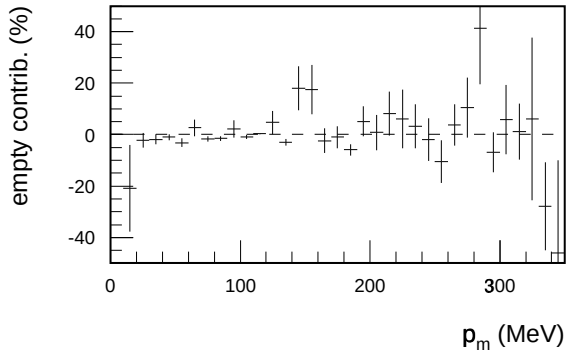

Figure 4.12: *Relative contribution of the cell wall to the total* $(e, e'pp)$ *yield for kinematics LQA as a function of the missing momentum. The empty-target data was analysed in the same manner as the* ^{3}He$(e, e'pp)$ *data.*

within the acceptance of the QDQ spectrometer for electron detection angles below approximately 30°. Under these circumstances, true ^{27}Al$(e, e'pp)$ events originating from these cell walls will contribute to the measured yield of $(e, e'pp)$ events. The contribution from these cell wall events has been reduced by limiting the y_{tg} acceptance of the spectrometer to ± 8 mm, as explained in section 4.1.

The contribution of cell wall events will be most prominent for kinematics LQ, where the spectrometer angle was set at 27.7°. To determine this contribution, dedicated measurements were performed with an empty target cell. The kinematic conditions were kept identical to those of the coincidence measurement. For the empty-cell measurements in the LQA kinematics, a charge of 15.6 mC was collected, which corresponds to more than 15% of the total charge collected on the ^{3}He gas in this kinematic setting. The contribution to the total yield (after applying the usual correction factors) originating from the cell walls was $1.4 \pm 0.7\%$ for the excitation energy region from -11 to 14 MeV, independent of the missing momentum p_m. The relative contribution from the cell walls to the corrected yield is shown in Fig. 4.12.

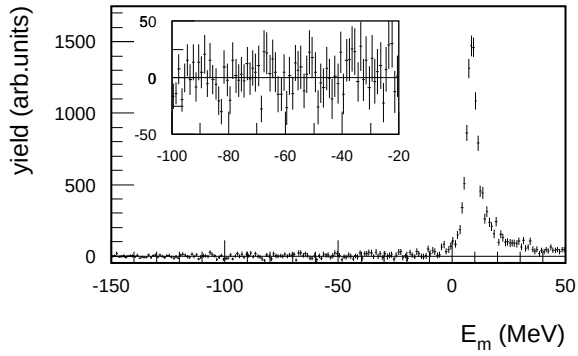

Figure 4.13: *Missing-energy distribution for kinematics LQA. The resolution amounts to 5.5 MeV (FWHM). The inset shows an enlargement of a subset of the same distribution. The yield in the E_m region between -100 and -20 MeV is -1.1 ± 1.7.*

Verification of the subtraction procedure

The proper subtraction of accidental coincidences is verified using the missing-energy distribution of the true $(e, e'pp)$ coincidences. Below the value corresponding to the two-proton separation energy, in this case the binding energy of ^{3}He, no true $(e, e'pp)$ events can occur. The strength in the region below this energy should be compatible with zero. For kinematics LQA, the missing-energy distribution for true $(e, e'pp)$ events is shown in Fig. 4.13. The peak corresponding to the three-body breakup of ^{3}He is located at E_m=7.7 MeV. The tail extending to higher E_m values is caused by energy loss suffered by the incident or scattered electron due to radiative processes. The inset shows an enlargement of the E_m distribution for the range $-100 < E_m < -20$ MeV. The yield in this region, -1.1±1.7, is compatible with zero.

4.4 From yield to cross section

The cross section for the reaction ^{3}He$(e, e'pp)$ is determined as a function of the kinematic quantities described in section 2.1, *e.g.*, ω, p_m, $p_{diff,1}$, or p_{ij}. The eight-fold differential cross section is defined as

$$\frac{d^8\sigma}{dV^8}(\Delta\boldsymbol{X}) = \int_{E_x} \frac{N(\Delta\boldsymbol{X})}{\int\mathcal{L}\,dt\,\mathcal{V}(\Delta\boldsymbol{X})} \left|\frac{\partial T_2}{\partial E_x}\right| dE_x. \tag{4.6}$$

In this equation, $\Delta\boldsymbol{X}$ refers to a range of values of (a set of) kinematic quantities in which the cross section will be represented, *e.g.*, $\Delta\boldsymbol{X} = (\Delta p_m, \Delta p_{diff,1})$. $\int\mathcal{L}dt$ represents the integrated luminosity, $N(\Delta\boldsymbol{X})$ the number of true $(e, e'pp)$ events, and $\mathcal{V}(\Delta\boldsymbol{X})$ the experimental detection volume in phase space. The factor $|\partial T_2/\partial E_x|$ is a Jacobian.

The integrated luminosity, $\int\mathcal{L}\,dt$, is the product of target thickness and collected charge. This collected charge was measured for each data file and summed. The density of the ^{3}He gas was determined by elastic scattering from ^{3}He (see section 4.5). The reduction of the target thickness due to the varying acceptance of the QDQ spectrometer along y (see section 4.1) is taken into account in the calculation of the experimental detection volume $\mathcal{V}$ and therefore the nominal thickness (*i.e.*, the density times the diameter of the cell) is used in determining the integrated luminosity.

The total ^{3}He$(e, e'pp)$ yield that contributes to the selected domain $\Delta\boldsymbol{X}$ is represented by $N(\Delta\boldsymbol{X})$. It takes into account the correction factors due to inefficiencies and incorporates the random subtraction:

$$N(\Delta\boldsymbol{X}) = \sum_i \frac{w_i(\tau_x, \tau_y)}{\epsilon_i}\, D(\boldsymbol{X}_i; \Delta\boldsymbol{X}), \tag{4.7}$$

where w_i accounts for the random subtraction, ϵ_i for the detector efficiencies and $D(\boldsymbol{x}; \boldsymbol{R})$ is a two-valued function, that has the value 1 if $\boldsymbol{x}$ is inside the region $\boldsymbol{R}$, and zero everywhere else. The sum $\sum_i$ loops over all three-fold coincident events inside the regions A, B, and C.

With the experimental setup used, not every interval $\Delta\boldsymbol{X}$ is equally likely to be hit. This detection volume $\mathcal{V}(\Delta\boldsymbol{X})$ in phase space is defined as

$$\mathcal{V}(\Delta\boldsymbol{X}) = \int D(\boldsymbol{X}'(\boldsymbol{v}); \Delta\boldsymbol{X}) D(\boldsymbol{v}; \boldsymbol{A})\, d\boldsymbol{v}. \tag{4.8}$$

In this equation, $\boldsymbol{X}'(\boldsymbol{v})$ is the vector of observables determined from the integration variable $\boldsymbol{v}$, $\boldsymbol{A}$ is the acceptance region of the combined three-detector setup, and the integration variable $\boldsymbol{v}$ represents $(\boldsymbol{p}'_e, \boldsymbol{p}'_1, \boldsymbol{p}'_2, y_{beam})$. The integration is carried out over the complete phase space. The dependence of $\boldsymbol{X}'$ on $\boldsymbol{v}$ is such, that the integration is best performed numerically.

Integration over the excitation-energy range

The quantity $N/\mathcal{V}$ of Eq. 4.6 is a nine-fold differential, $dT'_e\, d\Omega'_e\, dT'_1\, d\Omega'_1\, dT'_2\, d\Omega'_2$. To obtain the eight-fold differential cross section, it is integrated over the excitation energy E_x. This introduces a Jacobian, which in the $(e, e'pp)$ case can be expressed as:

$$\frac{\partial T_2}{\partial E_x} = \left[1 - \frac{E_2}{E_{rec}} \left(\frac{(\boldsymbol{q} - \boldsymbol{p}'_1) \cdot \boldsymbol{p}'_2}{|\boldsymbol{p}'_2|^2} - 1 \right) \right]^{-1}, \tag{4.9}$$

where E_2 and E_{rec} are the total energy of proton 2 and the recoiling neutron, respectively. As this Jacobian depends on the individual proton momenta, it is applied as a weight factor to the data on an event-by-event basis.

Not the entire region in E_x is integrated to determine the cross section as – except for resolution effects – the region below E_x=0 MeV does not contribute to the cross section for ^{3}He$(e, e'pp)$. To reduce the total statistical error due to the contribution of these events, the region $E_x < -11$ MeV is disregarded in the integration. This corresponds to more than 4σ from the position of the peak.

The events in the region at $E_x > 0$ MeV are due to true ^{3}He$(e, e'pp)$ events and include events of which either the incident or the scattered electron suffered energy loss due to the emission of photons, which results in a reconstructed E_x that is systematically larger. The shape of this radiative tail as a function of the excitation energy is readily calculated using the formalism of [MoT69].

The upper integration limit was set at E_x=14 MeV. For each kinematic setting, the fraction of events beyond this cutoff was calculated and applied as a correction factor to the data; they vary from 1.14 to 1.16.

In selecting this region in excitation energy, the uncertainty due to radiative effects on the other kinematic quantities is limited. The missing momentum p_m will be most strongly affected, but the variation is still limited to ± 4 MeV/c on average, which is smaller than the bin-width used in the presentation of the

cross section. The effect on the determination of γ_1 is estimated to be smaller than the angular resolution of the HADRON detectors.

Because of limitations imposed by the analysis software, the integration over the E_x interval is performed on the measured yield and the detection volume separately. As the variation of the detection volume $\mathcal{V}$ with E_x is small within the relevant range, its value is approximated by a constant $\tilde{\mathcal{V}}$ and taken out of the integration:

$$\frac{d^8\sigma}{dV^8}(\Delta \boldsymbol{X}) = \frac{1}{\int \mathcal{L}\, dt\, \tilde{\mathcal{V}}(\Delta \boldsymbol{X})\rfloor_{E_{equiv}}} \int_{E_x} N(\Delta \boldsymbol{X}) \left| \frac{\partial T_2}{\partial E_x} \right| dE_x. \tag{4.10}$$

The eight-dimensional volume $\tilde{\mathcal{V}}$ is evaluated at a specific value of E_x=E_{equiv}, such that the differential cross section, evaluated using equation 4.6 is identical to the cross section evaluated using Eq. 4.10. Due to the radiative tail of the distribution, this value does not correspond to E_x=0, but to a slightly higher value. This value was determined to be E_{equiv}=2 MeV and is identical for all kinematic settings, as the shape of the radiative tails is similar.

Determination of the experimental detection volume

To evaluate the detection volume $\tilde{\mathcal{V}}$, a numerical integration of equation 4.8 is performed. The generic code Q2HPHASPA is used, which evaluates the nine-dimensional integral for the volume spanned by the QDQ and both HADRON detectors using a Monte-Carlo method. The code determines $\mathcal{V}$ by

$$\mathcal{V}(\Delta \boldsymbol{X}) = \frac{N^{MC}(\Delta \boldsymbol{X})\, \mathcal{V}^{MC}}{N^{MC}_{total}}, \tag{4.11}$$

where $\mathcal{V}^{MC}$ is the volume of the hypercube, which can be calculated analytically. N^{MC}_{total} is the total number of samples drawn from the volume $\mathcal{V}^{MC}$, and $N^{MC}(\Delta \boldsymbol{X})$ the number of samples for which $\boldsymbol{X}'$ is within the volume $\Delta \boldsymbol{X}$.

For each detector, a momentum vector is generated randomly inside its acceptance from which relevant physical quantities $\boldsymbol{X}'$ are constructed. These Monte-Carlo events are sorted in intervals identical to the ones used in the projection of the measured data. The generated events originate from different positions along the beam line to account for the extended target. The volume $\tilde{\mathcal{V}}(\Delta \boldsymbol{X})$ is subsequently obtained by selecting a region ΔE_x having a width of

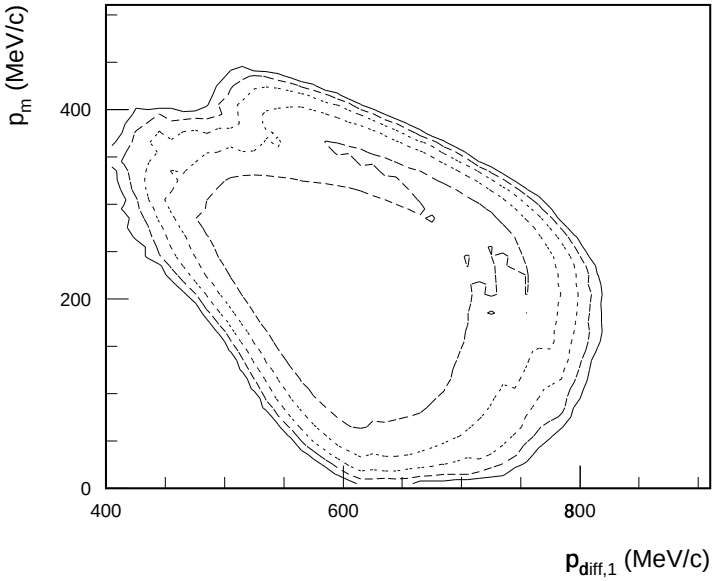

Figure 4.14: *Contour plot of the detection volume $\tilde{\mathcal{V}}$ as a function of $(p_m, p_{diff,1})$ for the combination of the kinematic settings LQA, LQV, and PEF. Contours are drawn at 30%, 10%, 3%, 1%, and 0.3% of the maximum value.*

10 MeV and centred around the equivalent energy E_{equiv}=2 MeV. This width is such that further reduction does not change the value of $\tilde{\mathcal{V}}$ by more than 1%. In Fig. 4.14, the volume $\tilde{\mathcal{V}}$ is shown for $\boldsymbol{X} = (p_m, p_{diff,1})$ for the combined kinematic settings at LQ.

In total 10^8 events were generated inside the nine-dimensional volume $\mathcal{V}^{MC}$ for every kinematic setting. This ensures that the contribution of the Monte-Carlo sampling error to the statistical uncertainty in the cross section is less than 0.4%.

QDQ volume

The angular acceptance of the QDQ is limited by an octangular slit with a central acceptance of ±70 mrad in both directions. However, the QDQ is not capable of viewing the entire length of the target with complete coverage of this angular

domain. As the QDQ is the only detector with such a limited y acceptance, the effective y acceptance of the $(e, e'pp)$ detection volume is accounted for by an effective solid angle of the QDQ.

Sample events are drawn uniformly inside a cone with an angular span of 85 mrad, originating from vertex positions $-25 < y_{beam} < 25$ mm. Using the parametrization of the QDQ acceptance, as described in section 4.1, the effective solid angle of the spectrometer is determined.

The energy acceptance along the focal plane is independent of the angles of the electron within the relevant domain and can therefore be generated uniformly over the X1 acceptance.

HADRON volume

The HADRON detector may be thought of as being composed of a large number of rectangular detectors. Every combination of H1 and L1, and H2 in itself represents an active detection element with a solid angle and an energy acceptance. This solid angle, which depends on the H1–H2 combination, can be calculated analytically. The energy acceptance, however, is more complicated, as it depends on the impact angle of the particle. Therefore, this acceptance is evaluated using uniformly distributed samples between the lowest possible energy (at an impact angle of zero degrees) and the largest possible one (at the maximal impact angle). The actual energy limits are thus predetermined for each active element. The extension of the target is taken into account in the calculation of the momentum vector by segmenting the extension of the target in eight regions of equal length. For each of these regions the aforementioned segmentation of the HADRON acceptance is performed. The angular acceptance of HADRON is such that no cutoff by the collimator is introduced in y_{tg}.

The treatment of HADRON in this way reduces the number of trigonometric computations and significantly increases the sample generation rate.

Normalization of the cross section

The integrated luminosity $\int \mathcal{L}\, dt$ is determined by both target thickness and collected charge. As stated earlier, the target thickness is derived from the gas density, by multiplication with the nominal length of the target in the beam direction. This has two advantages: the density can be compared between different

settings of the QDQ, and it allows a comparison of the density, as measured using elastic scattering from ^{3}He (section 4.5) with the one derived from the measured values for temperature and pressure (section 3.2).

The collected charge is measured using the beam-dump tank as a Faraday cup and integrating the current over time. As described elsewhere [Sta99b], this integration is affected by an offset current (I_0) and a multiplication factor (K_χ) that is duty-factor dependent. This duty-factor dependence was parametrized as

$$Q_{true} = Q\left(\frac{1}{1+p\chi}\right), \tag{4.12}$$

where the factor $p \approx 0.09$ is determined by a fit to dedicated calibration data taken with a beam of varying duty factor χ. In the present experiment, the duty factor was 80±10%. Hence, the correction factor K_χ amounts to 7.0±0.8%.

The offset I_0 was recorded during the experiment by measuring the instantaneous current in absence of an incident beam. The value of I_0 varied slightly during the experiment, from 15 nA at the start of the experiment to 40 nA at the end. However, the uncertainty on this value is rather large (±10 nA). The measured I_0 was verified using the amount of (e,e') events per measured unit charge for two different incident beam currents during the measurement of LQA. The value obtained in this way is 15±1 nA, which has been used to calibrate the I_0 measurements for the remaining kinematic settings. The slope of the current measurement was verified using a known current source; the measured deviation is less than 0.7%.

The systematic error to be associated with the current offset depends slightly on the average incident beam current, and typically amounts to 1.1%.

4.5 Determination of the target density

The thickness of the ^{3}He gas in the cell was determined by elastic scattering experiments performed in between the $(e,e'pp)$ data taking. Elastic ^{3}He(e,e') data were taken at each kinematic setting and the measured cross sections were compared to theoretical predictions. As the procedures, employed to determine the target density are the exact inverse of the methods used to determine the cross section for the $(e,e'pp)$ data, the systematic error associated with the

parametrization of the QDQ solid angle, will cancel out, as the effective solid angle of the QDQ was determined using the code Q2HPHASPA. Also the contribution of K_χ will cancel out, as the duty factor during the elastic and $(e, e'pp)$ measurements was similar. The uncertainty associated with the unfolding of radiative effects in the elastic-scattering measurements is estimated to be 1%.

The cross section for elastic scattering from ^{3}He can be expressed in the plane wave Born approximation as

$$\frac{d\sigma}{d\Omega} = \left(\frac{d\sigma}{d\Omega}\right)_{Mott} \frac{1}{1+q^2/4M^2} \left[\frac{q^2}{\boldsymbol{q}^2} F_C^2(q) + \frac{\mu^2 q^2}{2m^2 Z^2} \left(\frac{1}{2}\frac{q^2}{\boldsymbol{q}^2} + \tan^2\frac{\theta}{2}\right) F_M^2(q)\right], \tag{4.13}$$

where the Mott cross section contains the usual Z^2 and recoil factors, q^2 is $-Q^2$, $\boldsymbol{q}^2$ the three-momentum squared, μ is the magnetic moment of ^{3}He, M is the ^{3}He mass and m the nucleon mass.

The charge and magnetic form factors of ^{3}He, F_C and F_M, are taken from a SOG parametrization by Amroun *et al.* [Amr94] and converted to a 15-parameter Fourier-Bessel expansion (with a cutoff radius of 6.5 fm), which is a usable parametrization for the code MEFCAL. This code was subsequently used to calculate the cross section for charge scattering. To obtain the cross section due to magnetic scattering, the code was used with the parametrization of the magnetic form factor and its result was scaled with a global factor corresponding to the central kinematic setting. The ratio of the magnetic over the charge contribution varied between 2.3 and 13.7%.

The theoretical cross section was averaged over the acceptance of the spectrometer using the code CTXS. This code segments the angular acceptance of the spectrometer in 16 small squares and calculates the cross section for each square separately. The calculated cross section was also averaged over the contributing part of y_{tg}.

Figure 4.15 shows the reconstructed target density as derived from the elastic ^{3}He(e, e') measurements. As the variations are well within the statistical uncertainty, a constant target density of 53.7±0.5 mg/cm^3 has been assumed in the analysis of the $(e, e'pp)$ data. This density is independent of the vertex position along y, as verified by analysing the same data with varying limitations on y_{tg}. A constant nominal target thickness of 268±2.4 mg/cm^2 is therefore assumed.

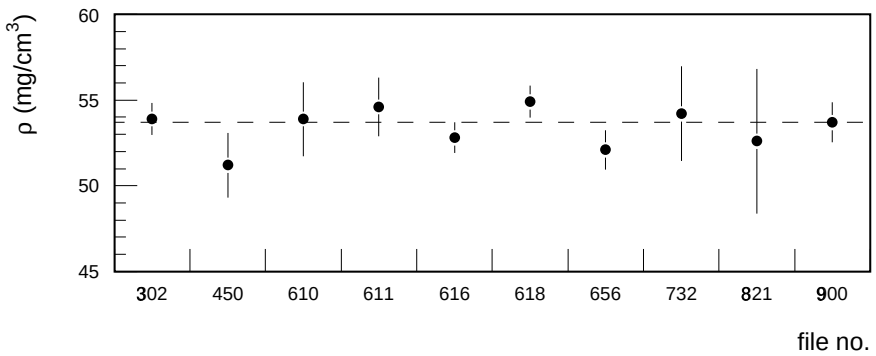

Figure 4.15: *Target gas density as determined by elastic scattering at various moments during the experiment. The dashed line indicates the average density (53.7±0.5 mg/cm^3) used in the determination of the $(e, e'pp)$ cross sections.*

The value of 53.7 mg/cm^3 is not consistent with the density as derived from the macroscopically measured temperature and pressure. These values, 15.1 K and 2.97 MPa, predict a density of 71 mg/cm^3. However, it should be noted that the temperature sensors were mounted close to the cold head and therefore do not reflect the temperature of the gas at the beam line. Assuming the pressure is correct (as it was calibrated before the start of the experiment), the reconstructed gas temperature at the interaction point is 20 K.

The effective target thickness is continuously monitored during $(e, e'pp)$ data taking by simultaneously measuring the number of (e, e') events per unit charge. This (e, e') yield is then related to measurement of the elastic scattering cross section by monitoring the prompt trigger yield in, *e.g.*, a HADRON detector. In this way, the target thickness during the measurement of an $(e, e'pp)$ kinematic configuration is linked to a neighbouring elastic (e, e') measurement. Fluctuations of the target thickness are less than 3%, as shown in Fig. 4.16.

The elastic (e, e') measurements are also used to determine the incident electron energy with high accuracy, as for elastic scattering the combined measurement of energy and angle of the scattered electron defines the kinematic configuration. The incident energy was reconstructed to be 563.7±0.3 MeV, where the

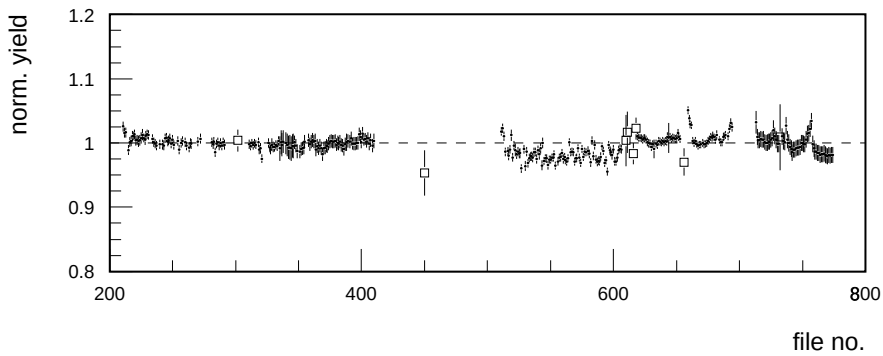

Figure 4.16: *Normalized yield of (e, e') events measured by the QDQ during $(e, e'pp)$ data taking. The (e, e') yield for each kinematic setting has been linked to a nearby elastic cross section measurement (the open squares) using the prompt trigger yield of the HADRON3 detector. The average of the elastic cross section measurements has been normalized to one. Deviations are less than 3%.*

uncertainty is mainly due to the momentum resolution and absolute calibration of the QDQ spectrometer.

4.6 Estimate of uncertainties

The statistical error on the cross section is determined by the uncertainty in the number of measured real events, in the estimated contribution of accidental events to the real-coincidence area A, and the uncertainty in the detection volume integration. The main contribution stems from the uncertainty on the number of real coincident events, as the number of measured accidental events is large and the corresponding weight factors f_B and f_C small. The increase of statistical uncertainty in the true yield, induced by the accidental contribution, varies from 1.15 (LQA) to 2.0 (HQ), as illustrated by Fig. 4.17. As argued in section 4.4, the contribution due to the uncertainty in the evaluation of the detection volume is less than 0.4%.

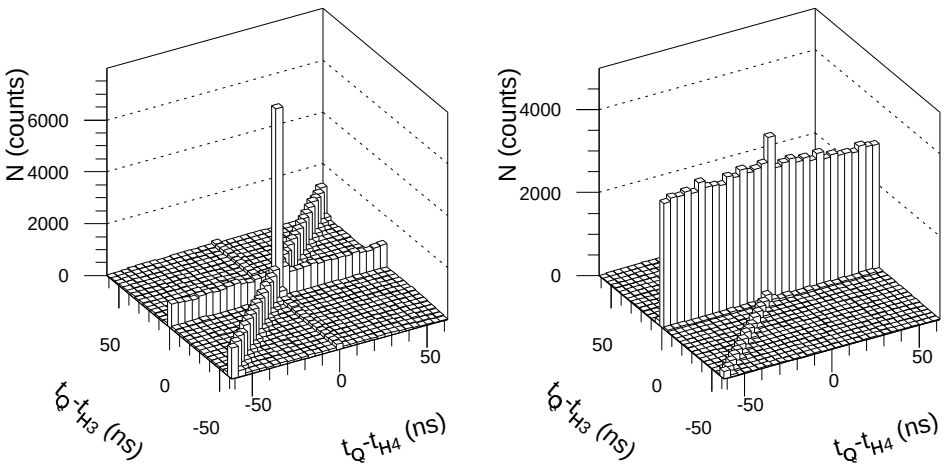

Figure 4.17: *Time difference distribution for three-fold coincident events. The left-hand panel shows the distribution for kinematics LQA, the right-hand panel for HQ.*

Besides the statistical uncertainty, a systematic uncertainty has to be associated with the measured cross section. The largest contribution stems from the estimate of the loss of protons due to interaction processes, which is estimated using a model description of the detector. The accuracy to which these are known is limited, as they are partially based on extrapolations from the GeV domain. Its contribution is estimated to be 3% per detector. Because the same code is used to estimate the interaction processes for both HADRON detectors, the uncertainties are added linearly.

The accuracy with which the target thickness is known, is determined by the error in the elastic (e, e') measurements, as most of the uncertainty associated with the duty-factor dependent current offset and the parametrization of the QDQ solid angle will cancel out. The remaining uncertainty is estimated to be 3%.

The integration of the incident electron current is hampered by a slowly varying offset and an unstable reading of this offset current. These effects induce an uncertainty of 1%.

Table 4.2: *Sources contributing to the systematic uncertainty to be associated with the measured* ^{3}He$(e, e'pp)$ *cross sections.*

source		uncertainty
target thickness determination		3%
offset current determination		1%
HADRON detector simulation	(3%+3%)	6%
correlated track live time	(1%+1%)	2%
aerogel detection threshold		0.5%
radiative tail cutoff		1%
cell wall contributions		1.5%
integration of the detection volume		1%
total systematic uncertainty		*7.4%*

Remaining contributions are due to the correlated track live time of the HADRON detectors (two times 1%, added linearly), the requirements imposed on the aerogel signal in the analysis (0.5%), the cutoff of the radiative tail (1%), the cell wall contribution (1.5%) and the determination of the detection volume $\tilde{\mathcal{V}}$ (1%). All contributions are listed in Table 4.2; they sum up quadratically to 7.4% in total.